

# **HiSST: 4th International Conference on High-Speed Vehicle Science Technology** 22 -26 September 2025, Tours, France



# A Novel Microwave Resonant Probe Diagnostic to Perform Real-Time and In-Situ Electron Density Measurements in Atmospheric Re-Entry Plasmas

Federico Boni<sup>1</sup>, Viviana Lago<sup>2</sup>, Benjamin Khiar<sup>1</sup>

#### Abstract

In this work, the design, manufacturing, and validation of a new high-frequency curling probe operating near 20 GHz is presented. This probe is capable of accessing electron densities in the  $10^{12} - 10^{14}$  cm<sup>-3</sup> range, typical of atmospheric re-entry plasmas. A new interpretation model, accounting for collisional effects in high-density plasmas, is developed and validated through 3D electromagnetic simulations of the probe frequency response. For the first time, the curling probe diagnostic is deployed in a highenthalpy supersonic plasma wind tunnel (PHEDRA facility at ICARE Laboratory in Orléans, France) to characterize electron density across the shock layer of a coin-shaped model under re-entry relevant conditions. Boron nitride protective coatings have allowed the probes to withstand cumulative plasma exposure of 30 minutes under thermal fluxes of 200 – 300 kW/m<sup>2</sup> and gas temperatures of thousand kelvins. Curling probe measurements provided integral electron densities across several millimeters of the shock layer, yielding values on the order of 10<sup>13</sup> cm<sup>-3</sup>. These results are in fair to good agreement with cylindrical Langmuir probe results and consistent with complementary direct Monte Carlo simulations of the plasma flow. These findings demonstrate the feasibility and robustness of curling probe for diagnosing high-density plasmas in re-entry conditions, highlighting their potential for advanced ground-based experimental campaigns and for future in-flight applications.

Keywords: electron density, microwave curling probe resonator, collisional plasma, supersonic flow, atmospheric re-entry

#### **Nomenclature**

CP - curling probe

CP20 – high-frequency curling probe

PLP - planar Langmuir probe

CLP – cylindrical Langmuir probe

DSMC - Direct Simulation Monte Carlo

RF - radio frequency

n<sub>e</sub> – electron density (cm<sup>-3</sup>)

 $f_r$  – probe resonance frequency in plasma (Hz)

 $f_0$  – probe resonance frequency in vacuum (Hz)

 $\alpha$  – curling probe calibration coefficient

 $\nu$  – total collision frequency (Hz)

 $\zeta_c$  – collision factor

 $\epsilon_n$  – plasma relative permittivity

 $\omega_n$  – plasma angular frequency (rad/s)

 $\omega$  – wave angular frequency (rad/s)

#### 1. Introduction

Accurate electron density measurement is crucial for understanding the plasma environment generated during atmospheric re-entry, where extreme thermal and aerodynamic conditions result in complex, high-temperature ionized flow around the spacecraft. As the vehicle descends into the atmosphere at

HiSST-2025-342 Page |1 A Novel Microwave Resonant Probe Diagnostic to Perform Real-Time and In-Situ Electron Density Measurements in

<sup>&</sup>lt;sup>1</sup> Physics Instrumentation and Space Department, ONERA, Université Paris-Saclay, 91123 Palaiseau, France, federico.boni@onera.fr

<sup>&</sup>lt;sup>2</sup>Laboratoire ICARE, CNRS, 1 C Av de la Recherche Scientifique, Orléans

hypersonic speeds, it compresses and heats the surrounding air, forming a bow shock. The shock-induced compression raises the gas temperature to several thousand kelvins, resulting in significant ionization of the flow and the formation of a plasma sheath enveloping the spacecraft. This plasma sheath can strongly affect telemetry, communication, and navigation. A particularly critical phenomenon is radio frequency (RF) blackout, in which the plasma surrounding the vehicle severely attenuates (or even blocks in worst case scenarios) electromagnetic wave propagation, impairing communication between the spacecraft and ground control. RF blackout occurs when the plasma frequency exceeds the operational frequency of the onboard communication systems. For Earth re-entry missions, RF blackouts lasting from several tens of seconds (e.g., during RAMC re-entries [1]) up to minutes have been observed, especially during peak heating conditions yielding strong flow ionization. Understanding and mitigating this blackout is vital for ensuring continuous data transmission and mission safety.

Robust electron density diagnostics are therefore essential for studying re-entry plasmas, validating numerical models, and help developing systems to minimize blackout effects. To date, most in-flight measurements have relied on microwave reflectometry [2], [3] and electrostatic probes [4]. Reflectometry, a non-intrusive line-of-sight technique, estimates plasma density from wave attenuation. The measurable density range and sensitivity can be adjusted by varying the wavelength, although this comes at the cost of spatial resolution. Electrostatic probes provide localized measurements but are intrusive due to their polarized electrode and require careful attention to interpretation models [4]. Microwave resonant probes offer a promising alternative: they are low intrusive, simple to implement, and provide good spatial and temporal resolution [5]–[7]. These probes are characterized by a resonance frequency that depends on the relative permittivity of the plasma, which is directly related to the electron density.

As part of the AMHYRA project funded by the Agence de l'Innovation de Défense, which investigates supersonic flow interactions with re-entry vehicles, we propose the use of the curling probe to provide accurate and real-time electron density measurements [6]. This novel microwave resonant probe is compact, has low power consumption, and can be flush-mounted into conductive walls or embedded within dielectric walls, making it suitable for both ground-based and in-flight applications. The present work investigates the extension of the curling probe diagnostic to high-density collisional plasma regimes characteristic of atmospheric re-entry, where electron density can reach up to 10<sup>13</sup> cm<sup>-3</sup> and collision frequency can be as high as 1 THz [2], [4].

The paper is organized as follows. Section 2 presents the curling probe principle, interpretation models, and the new design used in this work. Section 3 describes the experimental apparatus and numerical tools, including the supersonic test facility, and the scaled re-entry model. Section 4 presents preliminary results of electron density measurements collected with curling probes and Langmuir probes at the stagnation point of the scaled model. Finally, section 5 is the conclusion.

# 2. The curling probe

The curling probe (CP) consists of a spiral resonator capacitively coupled to a monopole antenna at its center (Figure 1, left). The probe is characterized by a resonance frequency that depends on the relative permittivity of the surrounding medium. In the case of a lossy dielectric medium ( $\epsilon_r > 1$ ), the resonance frequency shifts towards lower values. If the probe is immersed in a plasma with relative permittivity  $\epsilon_p < 1$  (Eq. 1), the resonance frequency shifts towards higher values. This behavior is illustrated in Figure 1 (right).

$$\epsilon_p = 1 - \left(\frac{\omega_p}{\omega}\right)^2 \tag{1}$$

where  $\omega_p = \sqrt{\frac{e^2 n_e}{m_e \epsilon_0}}$  is the plasma frequency,  $\omega$  is the angular frequency of the excitation signal applied to the probe, e and  $m_e$  are the electron charge and mass,  $n_e$  is the electron density, and  $\epsilon_0$  is the permittivity of free space.

An absolute calibration method of the probe frequency response allows for the accurate determination of the absolute electron density number from the measured frequency shift [6]:

$$n_e = \frac{4\pi^2 m_e \epsilon_0}{e^2} (1 + \alpha)(f_r^2 - f_0^2)$$
 (2)

Where  $f_r$  and  $f_0$  are the resonance frequencies in plasma and in vacuum, respectively, and  $\alpha$  is the calibration coefficient determined through an experimental calibration procedure using solid dielectric etalons of known permittivity. When necessary, electron density measurements can be corrected for the presence of the plasma sheath in front of the probe [8].

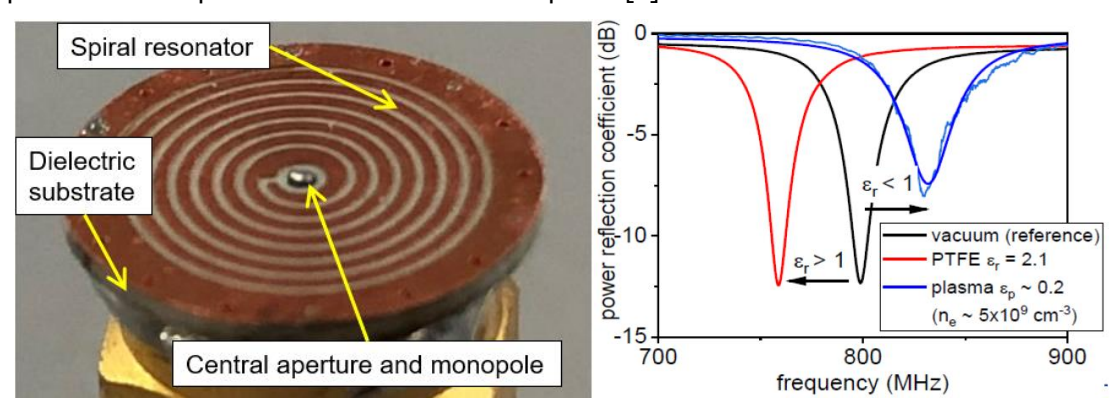


Figure 1. Left: photograph of an ONERA curling probe. Right: typical measurement of reflectance spectrum of a CP in vacuum (black line), in contact with a PTFE sample (red line), and immersed in a plasma (blue line).

Curling probe design and interpretation models have primarily been developed for low-pressure plasmas  $(10^{-4}-10\text{ Pa})$ , nearly-collisionless  $(\nu/\omega_p \lesssim 1)$ , where  $\nu$  is the collision frequency), and weakly-magnetized  $(\omega_{ce}/\omega \lesssim 1)$ , where  $\omega_{ce}$  is the electron cyclotron frequency) regimes. Such conditions are typical of reactive plasmas [5], [9], [10], and of electric propulsion devices [6]–[8], [11]. The ONERA conventional CPs have vacuum frequencies in the 0.7 - 3 GHz range, diameters between 6 – 10 mm, and a measurement uncertainty of about 20% over a density range from  $10^7$  to  $10^{11}$  cm<sup>-3</sup>.

## 2.1. Design of a high-frequency curling probe

Probe sensitivity and measurable density range primarily depend upon the vacuum frequency  $f_0$  [6]. Probe sensitivity is quantified by the coefficient  $K \stackrel{\text{def}}{=} \frac{\Delta f}{n_e} \propto \frac{1}{(1+\alpha)f_0}$ , expressed in MHz/10<sup>9</sup> cm<sup>-3</sup>. Higher sensitivity means that a given density will induce a larger frequency shift. Consequently, the minimum detectable density depends on both the probe sensitivity and the system resolution. In a typical experimental setup [6]–[8], the minimum measurable electron density can be estimated as

$$n_e^{MIN} \simeq \min\left(\frac{0.05\% \cdot f_0 [\text{MHz}]}{K}, \frac{1 \text{ MHz}}{K}\right)$$
 (in units of 10<sup>9</sup> cm<sup>-3</sup>)

The maximum measurable density can be approximated by

$$n_e^{MAX} \simeq 1.7 \times \left(\frac{f_0[\text{MHz}]}{897}\right)^2$$
 (in units of 10<sup>10</sup> cm<sup>-3</sup>) (4)

Using Eqs. 3 and 4, we have designed a high-frequency curling probe to access the high electron densities range ( $10^{12} - 10^{13}$  cm<sup>-3</sup>) typical of re-entry scenarios [2], [4]. This new probe, called CP20, has a vacuum frequency of ~20 GHz, a resonator length of 5 mm, and a diameter of 6 mm, as shown in Figure 2 (left). Prior to fabrication, its frequency response has been simulated using 3D numerical simulations in COMSOL Multiphysics (see section 3.4 for details), to ensure correct behavior under relevant plasma conditions. The simulated reflectance spectra of CP20 are shown in Figure 2 (middle): vacuum (black), in contact with PTFE (red), and immersed in a plasma with density  $10^{12}$  cm<sup>-3</sup> (blue). Experimental reflectance spectra of the manufactured CP20 (Figure 2, right) are in good agreement with simulations. Calibration of CP20 follows the method detailed in ref. [6].

Page |3
A Novel Microwave Resonant Probe Diagnostic to Perform Real-Time and In-Situ Electron Density Measurements in
Atmospheric Re-Entry Plasmas

Copyright © 2025 by author(s)

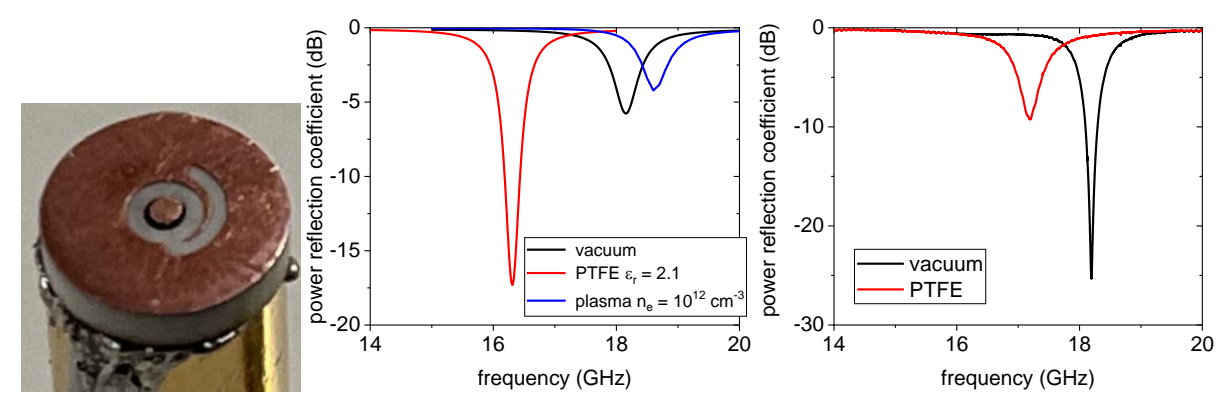


Figure 2. Left: newly designed CP20 prototype. Middle: simulated reflectance spectra of the CP20. Right: measured reflectance spectra of the manufactured CP20.

The table below summarizes the different curling probes currently available at ONERA and their measurement performance. We note that, for the same probe type, performance may slightly vary depending on the quality of the manufacturing process and surface coatings [6].

**Table 1.** Curling probes currently available at ONERA and their measurement performance.

Probe type	<i>K</i> (MHz/10 <sup>9</sup> cm <sup>-3</sup> )	$n_e^{MIN}$ (cm $^{ extsf{-3}}$ )	$n_e^{MAX}$ (cm <sup>-3</sup> )	Diameter (mm)
CP700	7	5x10 <sup>7</sup>	10 <sup>10</sup>	10
CP3000	1.2	1.7x10 <sup>9</sup>	3.4x10 <sup>11</sup>	8
CP20	0.25	4x10 <sup>10</sup>	9x10 <sup>12</sup>	6

## 2.2. Collisional interpretation model of the CP

Re-entry plasma regimes can be weakly collisional or collisional [2], [4]. The nearly-collisionless CP model (Eq. 2) can be modified to account for the presence of collisions in the plasma [7]:

$$n_e = \frac{4\pi^2 m_e \epsilon_0}{e^2} (1 + \alpha) (f_r^2 - f_0^2) \zeta_c$$
 (5)

where  $\alpha$ ,  $f_r$ ,  $f_0$  have the same definition as in Eq. 2, and  $\zeta_c$  is the collision factor, defined as

$$\zeta_c = \left(1 + \left(\frac{\nu}{2\pi f_*}\right)^2\right) \tag{6}$$

where  $\nu$  is the total collision frequency, accounting for both Coulomb and elastic collisions.

The evolution of  $\zeta_c$  with the collision frequency depends strongly on the probe vacuum frequency, as illustrated in Figure 3. Figure 3 (left) shows the variation of collision frequency  $\nu$  with altitude, computed using RAMC re-entry flight data [2], [4] using a normal shock approximation. The collision frequency decreases with altitude, from around 1 THz at 20 km to around 10 MHz at 100 km. Figure 3 (right) presents the variation of collision factor with  $\nu$  for low-frequency CPs ( $f_0 \sim 1$  GHz, black scatter points) and high-frequency CPs ( $f_0 \sim 20$  GHz, red scatter points). For both,  $\zeta_c \simeq 1$  when  $\nu \leq 1$  GHz, meaning that collisions can be neglected and the nearly-collisionless model (Eq. 2) is applicable. For  $\nu > 1$  GHz,  $\zeta_c$  increases significantly, by up to 4 orders of magnitude for low-frequency CPs. For high-frequency CPs, a substantial increase in  $\zeta_c$  is observed around  $\nu \simeq 1$  THz. In such regimes, the collisional model (Eq. 5) must be used to avoid significant underestimation of the electron density.

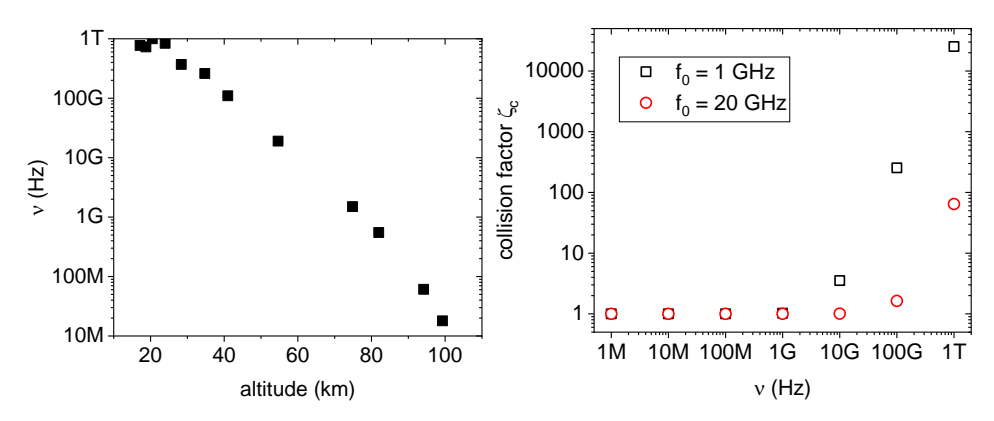


Figure 3. Left: evolution of collision frequency  $\nu$  with the altitude from RAMC data [2], [4] and normal shock approximations. Right: evolution of collision factor  $\zeta_c$  with collision frequency for two CP vacuum frequencies.

# 3. Apparatus and methods

# 3.1. The PHEDRA facility

The PHEDRA (Nonequilibrium Plasma Wind Tunnel for Atmospheric Reentry) facility is a high-enthalpy supersonic wind tunnel part of the Fast Platform located at CNRS laboratory ICARE in Orléans (France) [12], [13]. It consists of a cylindrical vessel 4.5 m long and 1.2 m in diameter, equipped with an arcjet fed by a 40 kW DC power supply. The facility can be used to reproduce aerothermodynamic properties of ionized gas flows with Mach numbers 1 – 8 at pressures between 1 and 10 Pa. The facility is equipped with optical ports, fluid, and electrical lines feedthroughs. A three-stage pumping system provides a total pumping speed of 26,000 m<sup>3</sup>/h, yielding a base pressure of 4 – 8 Pa. These conditions are representative of the re-entry regimes encountered at altitudes lower than 80 km.

The plasma source is an arc-jet generator equipped with a conical nozzle. The throat is made of tungsten, while the cathode incorporates a zirconium insert. Both components are water-cooled. In this work, the arc-jet source is operated with argon at around 30 V and 70-150 A, giving 2.2 - 4.4 kW plasma power.

#### 3.2. The model

The model used in this work is a coin-shaped disk (35 mm x 3 mm), with a 7.5 mm central hole for probe flush-mounting (Figure 4). Three different materials have been used: stainless steel (labeled as "A" in Figure 4), molybdenum (labeled as "Mo" in Figure 4), and MACOR. The coin-like geometry is selected for its simplicity in flush-mounting the diagnostic near the stagnation point, as well as for the simplicity it offers in numerical simulations.

The disk is bonded to an alumina supporting cylinder of 38 mm in diameter and 50 mm in length, using ceramic adhesive Resbond 905 (Figure 4, left). A thermocouple is embedded within each model to monitor the temperature during the experiments. Models are installed on a mechanical piston that allows them to be moved into and out of the jet. Two models can be installed at the same time. When one model is immersed in the plasma jet, the other one is completely outside, and vice versa. A third configuration allows to maintain both models outside the plasma jet (as illustrated in Fig. 6 of ref. [14]). The interaction of the supersonic plasma flow with the body is presented in Figure 4 (right), where the detached shock is clearly visible, indicating a large stand-off distance resulting from the low-pressure conditions.

HiSST-2025-342 Page |5 A Novel Microwave Resonant Probe Diagnostic to Perform Real-Time and In-Situ Electron Density Measurements in



Figure 4. Left: coin-like body mounted on the alumina supporting cylinder. Right: supersonic argon plasma flow interacting with the body.

# 3.3. Plasma diagnostics

Three plasma diagnostics have been used: a planar Langmuir probe (PLP), a cylindrical Langmuir probe (CLP), and a microwave resonant curling probe (CP).

The planar Langmuir probe (PLP) is used to measure the electron density and temperature at the surface of the disk. The probe consists of a 4 mm-diameter tungsten planar cylinder, flush-mounted on the MACOR disk, as shown in Figure 5 (left).

The cylindrical Langmuir probe (CLP) is used to measure the electron density and temperature in both the shock layer and the free stream. The probe consists of a 200  $\mu$ m tungsten wire, 3 mm in length, supported by a 1 mm alumina tube, as illustrated in Figure 5 (middle).

Both Langmuir probes are biased with a triangular voltage signal, whose amplitude can be adjusted to match the plasma conditions, and the probe current is recorded through a shunt resistor. A comparison of the I-V characteristics obtained with the PLP (black curve), the CLP in the shock layer (blue curve), and the CLP in the free stream (red curve) is shown in Figure 5 (right).

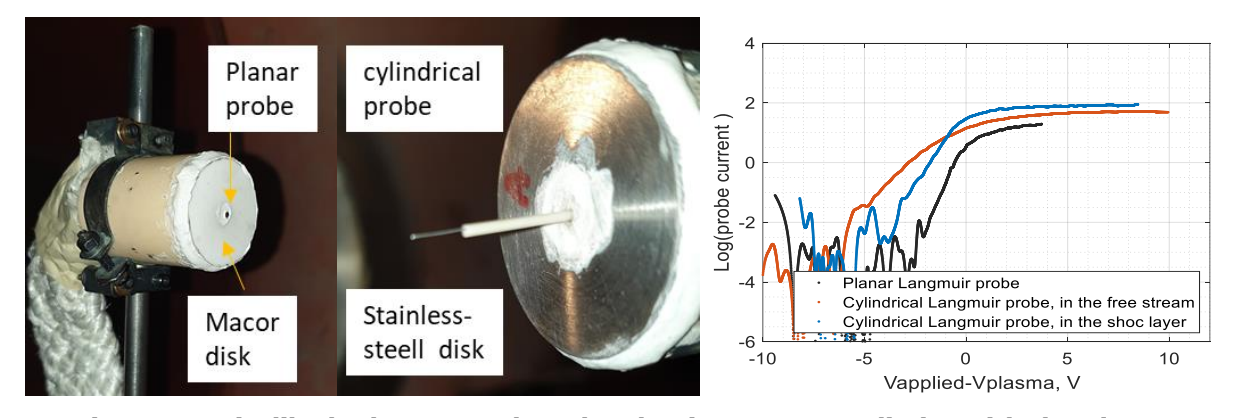


Figure 5. Coin-like body mounted on the alumina support cylinder with the planar Langmuir probe (left) and with the cylindrical Langmuir probe (middle). Right: comparison of the planar and cylindrical probes I-V characteristic (150 A, 0.47 g/s).

The collisionless theory developed by Laframboise is applied to analyze the I-V characteristics and to determine the corresponding local electron properties. This approach is suitable here since the experiments are performed at low pressure (~4 Pa), where the electron mean free path is large compared to probe dimensions, and collisional effects can be neglected.

The distance of the model from the nozzle exit is fixed at 9 cm for all measurements presented in this paper. Flow visualization has been performed using a Kuro camera, which is a back illuminated CMOS camera, to analyze the shock position under the different experimental conditions. Based on these observations, two probe measurement locations were selected: 4.5 mm within the shock layer and 16.8 mm in the free stream. Figure 6 shows two images captured with the Kuro camera, illustrating the interaction of the disk with the plasma flow at plasma condition I = 150 A and  $\dot{m} = 0.47 \text{ g/s}$ . The images highlight the shock layer around the disk and the CLP positioned within the shock boundary layer (left image) and in the free stream (right image).

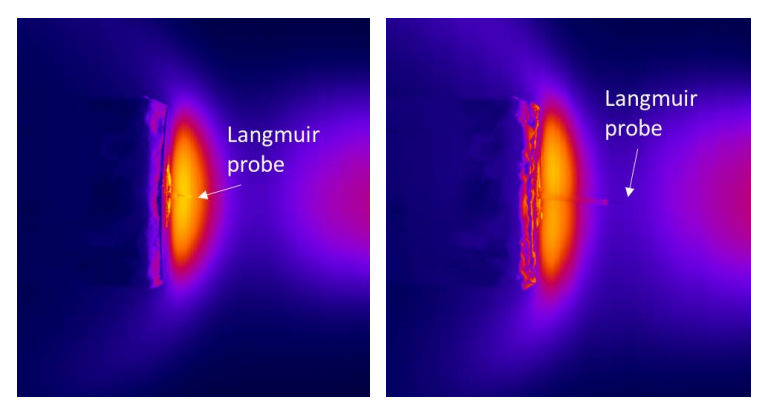


Figure 6. Shock around the coin-like body with the cylindrical Langmuir probe positioned in the shock boundary layer (left) and in the free stream (right).

The microwave resonant probe used in this work, (i.e., the CP20 described in section 2.1) is coated with a boron nitride spray coating for thermal protection up to 1000 °C (see Figure 7, left). Without this protection, the copper resonator surface would most probably degrade under high-temperature conditions and plasma sputtering. The CP is flush-mounted into the coin-like model such that the resonator surface of the probe is co-planar with the model surface (Figure 8, left). The probe mounted on the stainless-steel model is referred to as CP20A ( $f_0 \sim 15.4$  GHz,  $\alpha \simeq 46$ , K = 0.06 MHz/ $10^9$  cm<sup>-3</sup>), while the one mounted on the molybdenum model is designated CP20B ( $f_0 \sim 15$  GHz,  $\alpha \simeq 93$ , K = 0.04 MHz/ $10^9$  cm<sup>-3</sup>). Electron density is computed using the nearly-collisionless model (Eq. 2), since under flow conditions of this work the collision frequency (estimated at 0.1 - 1 GHz) yields a collision factor (Eq. 6) effectively equal to 1 for the CP20 operating near 20 GHz.

Reflectance spectra are acquired using a Rohde & Schwarz ZNB20 vector network analyzer (VNA) operated in swept frequency mode [6]. For all measurements, the VNA intermediate frequency filter bandwidth is set to 10 kHz and the frequency resolution is 0.8 MHz, resulting in an acquisition time of ~1.3 s per spectrum. For each plasma condition, five consecutive CP measurements are performed to evaluate measurement uncertainty, reproducibility, and repeatability, while limiting the total exposure of the probe to high thermal fluxes (~200 - 300 kW/m² [13]). Each density data point presented in this paper and collected with CPs thus corresponds to the average of five consecutive measurements. The microwave feeding line between the VNA and the CP is calibrated for absorption and reflection using a standard open-short-matched procedure. It consists of two microwave cables with a total length of 3 m, connected via SMA connectors and including a coaxial vacuum feedthrough. The cables used here are specified up to 16 GHz; operating them near this upper limit degraded spectral quality even after calibration. This is shown in Figure 7 (right), which compares CP20A reflectance spectrum obtained when the probe is mounted inside the facility and connected through the full microwave line (blue curve) with that obtained when it is connected directly to the VNA port (orange curve). The highfrequency wavelets visible in the blue spectrum are attributed to cable performance limitations (transmission loss, absorption, and reflections). Importantly, the resonance frequency itself is only marginally affected. The error budget is calculated using the approach detailed in ref. [6]. For CP20A and CP20B, the measurement uncertainty is below 10% for electron densities larger than 5x10<sup>11</sup> cm<sup>-3</sup>. Figure 8 shows the condition of the stainless steel and molybdenum disks, together with the CP20A and CP20B probes, after several hours of operation in the PHEDRA facility. Although the BN coating was largely removed by the end of the tests, it enabled the probes to withstand a cumulative plasma exposure of about 30 minutes, during which they remained fully operational. The maximum probe temperature reached 140°C. These results demonstrate, for the first time, the applicability of the curling probe to re-entry conditions characterized by high plasma densities and very high thermal fluxes (~200 - 300 kW/m<sup>2</sup> [13]).

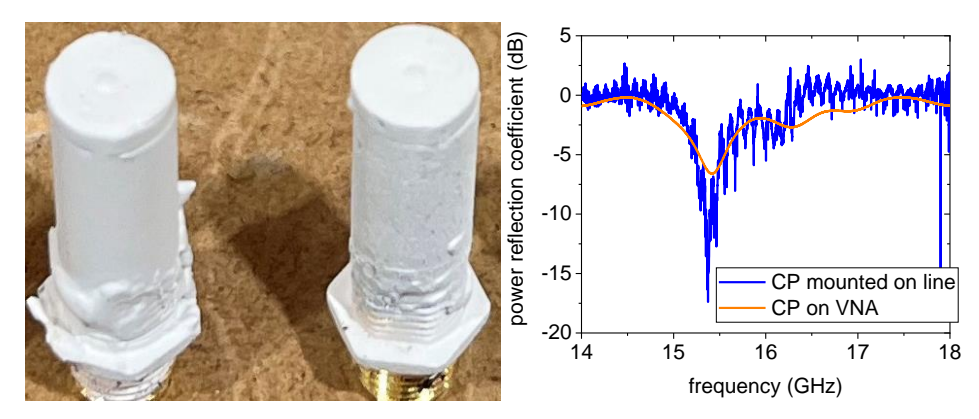


Figure 7. Left: the two CP20 coated with boron nitride spray used in the stainless steel and molybdenum disks. Right: comparison between the reflectance spectra measured with the CP mounted inside the facility through the line and the CP directly connected to the VNA.



Figure 8. Stainless steel and molybdenum disks and CP20A and CP20B after approximately 30 minutes of cumulative time exposure to plasma jet.

#### 3.4. 3D numerical simulations of the curling probe

The effects of Coulomb and elastic collisions are investigated through 3D numerical simulation using COMSOL Multiphysics, employing frequency sweep studies. Conductor boundaries are modeled as perfect electric conductors, and the excitation signal is injected into the probe via a 50  $\Omega$  coaxial port. Scattering boundary conditions are applied to the outer surfaces of the simulation domain (the "ambient box" of Figure 9) [6]. The finite element electromagnetic solver computes the power reflection coefficient (S11) at the coaxial port by solving the wave equation throughout the simulation domain. The resulting S11 spectra are fitted with a Lorentzian function to extract the resonance frequency (as illustrated in Figure 9, right). To balance accuracy and computational efficiency, the mesh is refined to maintain approximately 10 elements per wavelength, resulting in simulation runtimes of tens of hours per 50 frequency points. The plasma is modeled as a lossy-dielectric medium with a complex permittivity given by [15]

$$\epsilon_p = 1 - \frac{\omega_p^2}{\omega(\omega - i\nu)} \cdot \bar{\bar{I}} = [\epsilon_p' - j\epsilon_p''] \cdot \bar{\bar{I}}$$
 (7)

where  $\bar{l}$  is the identity tensor, and  $\epsilon'_p$  and  $\epsilon''_p$  represent the real and imaginary parts of the plasma relative permittivity, respectively. The simulation setup is shown in Figure 9 (left). The region labeled "analyzed medium" (blue domain) is assigned the collisional plasma permittivity as defined in Eq. 7, while the surrounding "ambient box" is assigned the permittivity of vacuum. Figure 9 (right) presents the simulated power reflectance spectra for the CP20 probe in 17-20 GHz frequency range. Scatter points corresponds to frequency values obtained from simulation, while solid lines represent the Lorentzian fits used to extract the resonance frequencies.

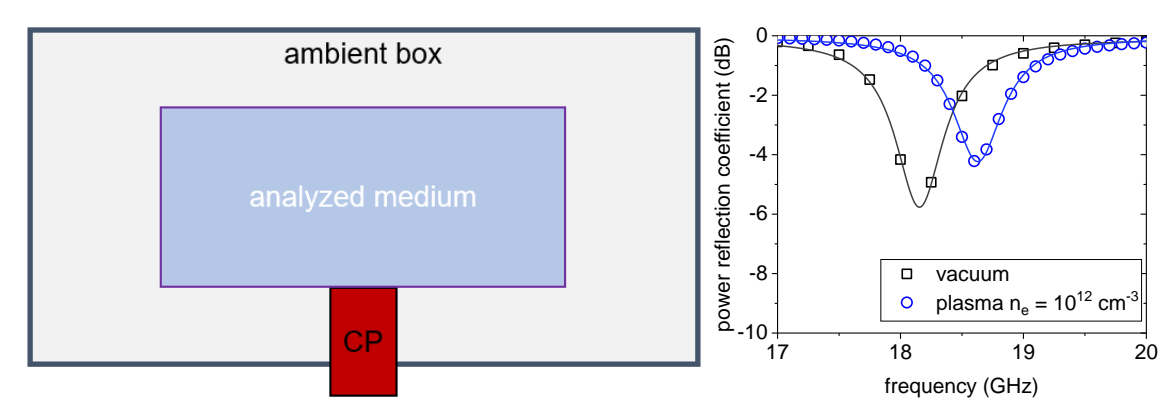


Figure 9. Left: simulation setup used in this work. Right: simulated spectra of a CP20 in vacuum (black line) and plasma (blue line).

#### 3.5. Direct Simulation Monte Carlo simulations

To complement the experiments, two-dimensional axisymmetric (r-z) direct simulation Monte Carlo (DSMC) simulations have been conducted using the SPARTA code [16], [17] to model the interaction of a high-temperature, high-velocity argon plasma with the coin-shaped body described previously. A simplified three-species plasma (Ar, Ar+, and  $e^-$ ) is considered. The simulations utilize a Variable Soft Sphere (VSS) "collision-averaged" model with parameters from ref. [18]. The free stream flow temperature is set to 2500 K, with a mean bulk velocity of 3500 m/s along the z-axis. A series of simulations was performed, varying the total particle number density from  $1.3 \times 10^{14}$  cm<sup>-3</sup> to  $6.5 \times 10^{14}$  cm<sup>-3</sup> and the electron fraction from 0.3% to 2.3%, corresponding to free stream electron densities ranging from  $10^{12}$  cm<sup>-3</sup> to  $3 \times 10^{12}$  cm<sup>-3</sup>. We acknowledge a limitation of the VSS model used in this study, as its "collision-averaged" approach is known to exhibit reduced accuracy at high ionization degrees. A "collision-specific" model would be more appropriate [19], but its implementation in SPARTA lies beyond the scope of this work.

The simulations employ the ambipolar approach available in SPARTA to circumvent the extremely short timescales associated with electron dynamics. The ratio of physical to simulation particles is selected to ensure at least about 30 ambipolar Ar+ ions per cell. Due the relatively low electron fractions, each cell contains > 100 neutral argon particles. A simple diffusive reflection model is used for wall interactions, with a fixed surface temperature of 1000 K and an accommodation coefficient of 1. Ambipolar Ar+ ions are assumed to fully recombine upon surface impact, releasing ~15.76 eV (the first ionization energy of argon). A simplified two-reaction model (electron impact ionization and three-body recombination [20], [21]) has been tested, but its influence is negligible under the studied conditions. The simulation domain is a  $50.75 \times 72.5 \text{ mm}$  (r-z) box discretized into  $210 \times 300 \text{ cells}$ , giving a uniform spatial resolution of dx~242 µm. Within the modeled free stream density range at 2500 K, the Ar-Ar mean free path (mfp) ranged from ~2 to 20 mm, resulting in a free stream dx/mfp ratio  $\leq 0.12$ . The simulation time step is set to dt = 10 ns. For the highest density case, the neutral collision time is  $\tau_{\text{coll}} \approx 1.6 \, \mu_{\text{S}}$ , giving a free stream dt/ $\tau_{\text{coll}}$  ratio of ~6x10<sup>-3</sup>. The CFL-like condition is satisfied, with V·dt/dx  $\approx 0.14$ .

An example of electron density profiles obtained with the SPARTA code and used in the interpretation of experimental data is shown in Figure 14. Future work will leverage the experimental database presented here to refine DSMC simulation for improved predictive capability.

#### 4. Results

This section presents (i) numerical results of the CP behavior in the presence of a collisional plasma and the numerical validation of the collisional model presented in Eq. 6, and (ii) experimental density measurements obtained with the curling and Langmuir probes in the PHEDRA facility.

## 4.1. 3D numerical simulations of the CP20 in a collisional plasma

Figure 10 shows results from 3D COMSOL simulations of the CP20 probe immersed in a collisional high-density plasma. Figure 10 (left) shows the reflectance spectra in three cases: vacuum (black line), collisionless plasma with  $n_e = 2 \times 10^{12}$  cm<sup>-3</sup> (red line), and collisional plasma with the same density with

 $\nu$  = 100 GHz (blue line). Increasing collisionality reduces the resonance frequency shift by nearly a factor of 2 (from about 910 to 520 MHz) and broadens the spectrum by a factor of ~3.5 (from 270 to 1000 MHz). This broadening corresponds to a lower quality factor, caused by additional energy losses from collisions, represented by the imaginary part of the plasma permittivity (Eq. 7).

Figure 10 (middle) reports the electron density retrieved from the simulated spectra using both the collisionless (Eq. 2) and collisional (Eq. 5) models, for a fixed plasma density of  $2x10^{12}$  cm<sup>-3</sup> and varying collision frequency  $\nu \in [10 \text{ MHz}, 1 \text{ THz}]$ . Below 10 GHz, both models converge to nearly identical values, confirming that collisions have negligible impact in this regime. This is consistent with the real (black) and imaginary (red) parts of the plasma permittivity shown in Figure 10 (right): the real part remains constant at ~0.5, and the imaginary part stays close to zero. For collision frequencies between 10 – 200 GHz, the collisionless model (blue points) increasingly underestimates the density, while the collisional model yields results within  $\pm 20\%$  of the true input value. This divergence is explained by the evolution of permittivity: the real part increases from ~0.5 to ~0.88, while the imaginary part rises to 0.2-0.25, indicating strong wave damping. At very high collision frequencies ( $\nu = 1 \text{ THz}$ ), both models fail to recover the correct density, with output values close to zero. In this regime, the plasma permittivity approaches that of free space: the real part increases to ~0.994, and the imaginary part decreases to 0.05. Consequently, the frequency shift between vacuum and this highly-collisional plasma becomes almost zero, rendering the probe insensitive to the plasma.

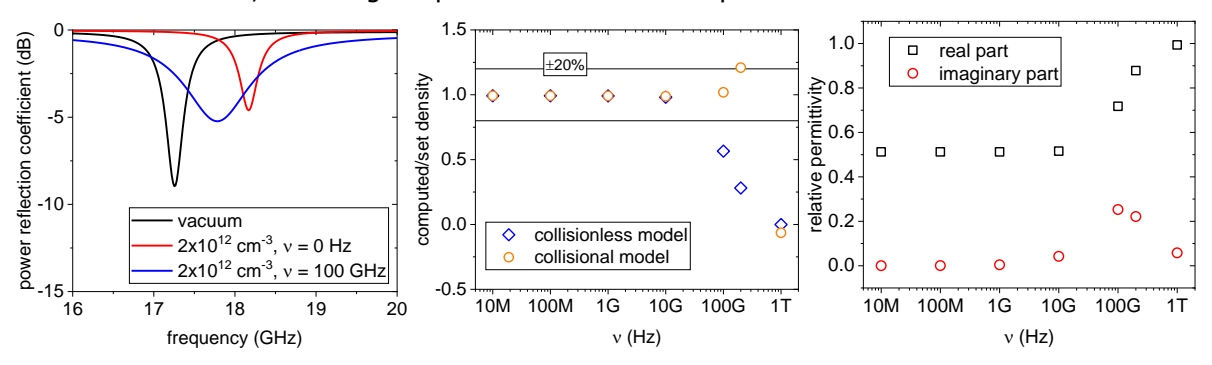


Figure 10. Left: simulated reflectance spectra of CP20 in vacuum (black), in plasma with no collisions (red), and in plasma with  $\nu=100$  GHz (blue). Middle: retrieved density obtained from numerical simulations of the CP20 exposed to collisional plasma. Right: real and imaginary part of plasma permittivity  $\nu s$  collision frequency.

#### 4.2. Electron density measurements inside the PHEDRA facility

In this work, the arc-jet source has been operated with argon under the conditions summarized here below.

Arc current, I <sub>arc</sub> (A)	Arc voltage, V <sub>arc</sub> (V)	Flowrate, m (g/s)	Power, Pel (kW)	Freestream pressure, p <sub>free-stream</sub> (Pa)
71	29.9	0.3	2.13±1.2%	3.05
71	31.1	0.47	2.2±1.8%	2.16
71	32	0.8	2.3±3.5%	2.14
100	29.5	0.3	2.95±0.7%	2.65
100	31.1	0.47	3.1±2.8%	2.07
150	30.1	0.47	4.5±1.2%	4.36

**Table 2.** Plasma operating conditions of the arc-jet source in the PHEDRA facility.

Figure 11 (left) shows typical reflectance spectra of the CP20A measured during the experimental campaign at ICARE laboratory in the PHEDRA facility. The black line is the spectrum in vacuum, while the blue line corresponds to the probe in the plasma jet. Lorentzian fits of the raw data are also shown. The resonance frequency shifts from 15.4 GHz in vacuum to 17.3 GHz in the plasma, corresponding to an electron density of  $\sim 2 \times 10^{13}$  cm<sup>-3</sup>. Figure 11 (right) compares single-shot measurements (orange squares) with averaged values obtained over five consecutive measurements (green diamonds) for each plasma condition for the CP20A. The single-shot measurement uncertainty is  $\sim 3-5\%$ ,

corresponding to an absolute uncertainty of  $\sim 1 \times 10^{12}$  cm<sup>-3</sup> for CP20A and  $\sim 4 \times 10^{12}$  cm<sup>-3</sup> for CP20B. The standard deviation over five consecutive measurements, accounting also for measurement uncertainty, can reach  $4 \times 10^{12}$  cm<sup>-3</sup> for CP20A and  $10^{13}$  cm<sup>-3</sup> for CP20B. These  $\sigma$ -values define the error bars in Figure 12 for the CP20A and CP20B datasets.

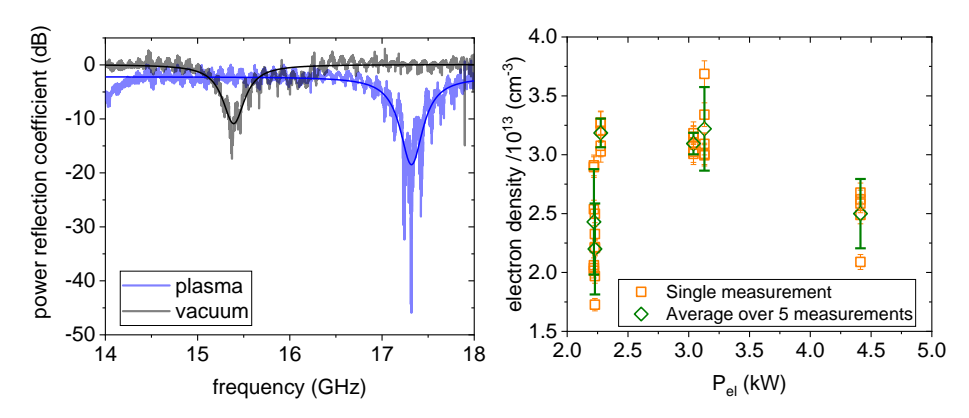


Figure 11. Left: typical CP20A reflectance spectra measured in vacuum and in plasma. Right: single-shot measurements (orange squares) and averages over 5 consecutive measurements (green diamonds) of electron density collected with CP20A.

Figure 12 shows the electron density and temperature determined using Langmuir and curling probes at a 9 cm distance from the nozzle exit, plotted against discharge power from Table 2. CP20A (black squares), CP20B (red circles), cylindrical Langmuir probe (CLP) across the shock layer (green triangles), cylindrical Langmuir probe (CLP) in the free stream (blue triangles), and planar Langmuir probe (PLP) at the disk surface are shown.

For all plasma discharge powers, Langmuir probe measurements indicate significant spatial variation of electron density across the shock layer. Density values increase from a few  $10^{13}$  cm<sup>-3</sup> in free stream to close to  $10^{14}$  cm<sup>-3</sup> in the shock layer (on average by a factor of 2 to 3) and decrease sharply at the disk surface down to a few  $10^{12}$  cm<sup>-3</sup>. Electron temperatures are higher at the disk surface (2 – 3 eV for 2 – 3 kW, decreasing to < 2 eV at 4.5 kW) and lower upstream the shock layer (0.5 – 0.7 eV). The higher electron temperatures at the disk surface are likely caused by selective survival of high-energy electrons overcoming the surface potential barrier. Increasing discharge power raises electron density while slightly decreasing electron temperature due to thermalization. This behavior is only weakly noticeable, as the variation in the electrical power of the plasma discharge remains modest.

Curling and Langmuir probe density trends are globally consistent, ranging from a few  $10^{13}$  to  $10^{14}$  cm $^{3}$ . CP20A density values fairly agree with CLP values measured in the free stream across all powers, whereas CP20B aligns better with CLP shock layer values. A good agreement between CP20A and CP20B density measurement is found for 3 kW of power; discrepancies up to a factor of 2 – 3 appear at 2 and 4.5 kW.

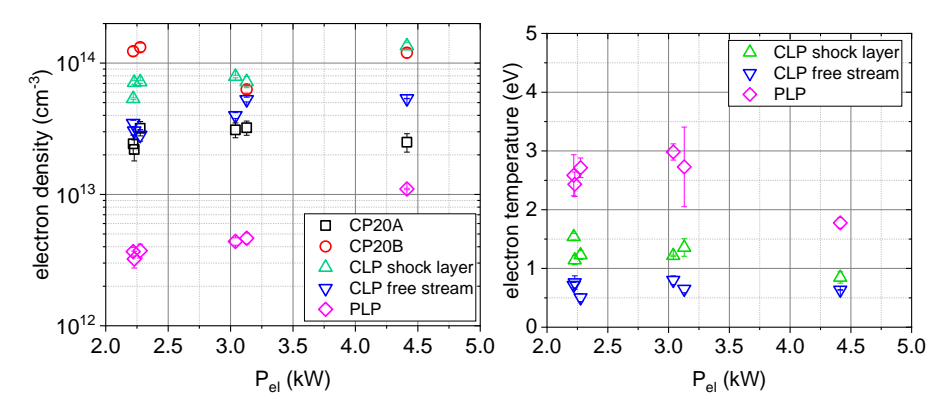


Figure 12. Left: electron density measurements collected with the CP20A, CP20B, cylindrical LP (shock layer and the free stream), and planar LP (disk surface). Right: electron temperature measurements collected with the cylindrical and planar LP.

It is important to highlight that both curling and cylindrical Langmuir probes provide integrated measurements: CPs over a length of about 5 - 10 mm [8] and CLPs over ~ 3 mm (i.e., the probe tip length). Only the planar LP provides quasi-local measurements, since its effective collection area is limited by the sheath, estimated to be in the  $100 - 500 \, \mu m$  range in the plasma conditions of this paper. The integration region of the CPs (red rectangle) and cylindrical LPs (black rectangle) is highlighted in Figure 13 which shows the light intensity profiles collected with the Kuro camera along the disk-shock axis for the six plasma conditions, normalized to the value at the disk surface. The light intensity is used here as a proxy to qualitatively trace electron density. A maximum occurs 2 and 3 mm from the disk, corresponding to the boundary layer, decreasing to a minimum at the shock end. This figure also reveals a relatively large stand-off distance, ranging between 14 and 15 mm, which can be attributed to rarefaction effects associated with the low chamber pressure (2-5 Pa). CP integration region (red rectangle in the figure) potentially covers varying density regions, whereas cylindrical LP (black rectangle) primarily probes either the high-density shock region or the free stream. We note that the CP probed region may be influenced by the probe coating and manufacturing process, such that even CP20A and CP20B, although nominally identical, could exhibit slightly different integration lengths. In future experiments, the probing regions of the probes will be carefully characterized prior to use.

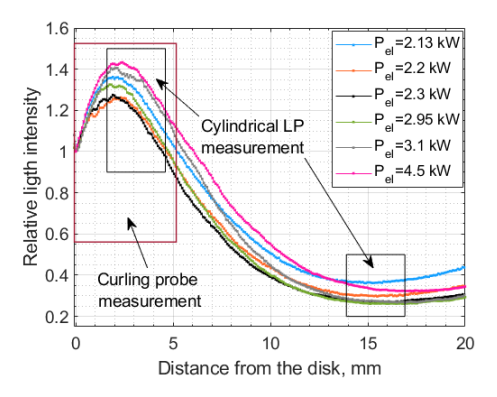


Figure 13. Kuro camera light intensity profiles normalized to disk surface intensity.

Finally, 3D COMSOL simulations, fed with DSMC/SPARTA electron density profiles across the shock layer, have been performed to assess CP frequency response in the presence of a spatially-varying density profile (Figure 14). DSMC simulation conditions are summarized in the table below.

Table 3.	Electron density profiles obtained from SPARTA simulations and fed into COMSOL simulations
	of the CP20.

Input profile	Freestream neutral density (cm <sup>-3</sup> )	Freestream electron density (cm <sup>-3</sup> )	Recombination at wall
1	1014	3x10 <sup>12</sup>	Yes
2	10 <sup>14</sup>	1x10 <sup>12</sup>	Yes
3	1014	1x10 <sup>12</sup>	No

Figure 14(a) shows the electron density profiles obtained from SPARTA DSMC simulations. The x-axis is the distance from the disk surface, and the y-axis is the electron density. Profiles obtained with wall recombination (profiles 1 and 2) exhibit a steep density increase from the disk surface up to  $\sim$ 2-3 mm, where the density reaches a maximum, followed by a gradual decrease farther from the disk. This trend aligns well with the experimental light emission profiles shown in Figure 13. The maximum density is approximately 3x the free stream density: around  $8.5 \times 10^{12}$  cm<sup>-3</sup> vs  $3 \times 10^{12}$  cm<sup>-3</sup> for profile 1 and around  $2.9 \times 10^{12}$  cm<sup>-3</sup> vs  $1 \times 10^{12}$  cm<sup>-3</sup> for profile 2. This is consistent with the experimental light emission, which rises from  $\sim$ 0.4 in the free stream to 1.4 at the peak (a 3.5-fold increase), and with electron density, which increases from  $\sim$ 4x10<sup>13</sup> cm<sup>-3</sup> in the free stream to  $\sim$ 10<sup>14</sup> cm<sup>-3</sup> across the shock, corresponding to a  $\sim$ 2.5-fold increase. Profile 3 (blue profile), obtained without wall recombination, shows a monotonically decreasing density profile with its maximum at the disk surface. Figure 14(b) presents

the COMSOL-simulated spectra of the CP20 response in the presence of profiles 1, 2, and 3, including the vacuum spectrum (black line) for reference. Frequency shifts on the order of a few GHz are obtained, comparable to experimental observations (Figure 10). Electron densities inferred from these shifts are shown in Figure 14(c) (brown squares):  $\sim 6 \times 10^{12}$  cm<sup>-3</sup> for profile 1,  $\sim 2 \times 10^{12}$  cm<sup>-3</sup> for profile 2, and  $\sim 10 \times 10^{12}$  cm<sup>-3</sup> for profile 3. These values closely match the spatially averaged density over 5 – 10 mm from the probe surface, corresponding to the approximate probed region of the CP20A and CP20B used here. We remind that a more precise determination of their probed region would require additional numerical simulations [8].

These results indicate that (i) the frequency shifts observed experimentally correspond to electron densities on the order of  $10^{13}$  cm<sup>-3</sup>, (ii) CP measurements in this configuration effectively provide an integral average over 5-10 mm, spanning the shock layer, and (iii) the maximum density across the shock layer likely occurs a few millimeters upstream of the disk surface.

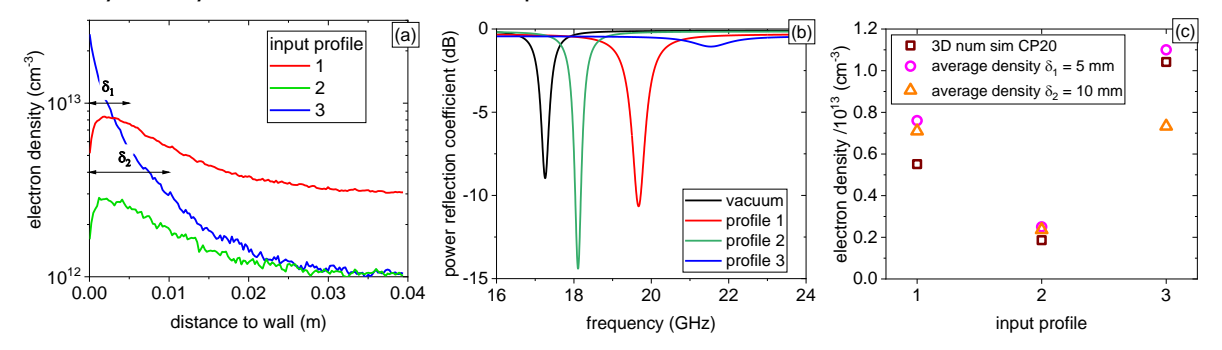


Figure 14. (a) Electron density profiles around the symmetry axis of the coin-like model obtained with SPARTA DSMC simulation code. (b) Simulated reflectance spectra of a CP20 in contact with density profiles in (a). (c) Inferred electron density from the frequency shifts in (b).

## 5. Conclusion

In this work, we have designed and manufactured a new high-frequency curling probe (CP20) operating around 20 GHz, capable of accessing electron densities in the  $10^{12}-10^{14}~\rm cm^{-3}$  range, typical of atmospheric re-entry plasmas. A new interpretation model has been developed to account for collisional effects in dense plasmas, and its validity has been confirmed through 3D COMSOL numerical simulations of the probe response.

For the first time, the curling probe diagnostic has been deployed in a supersonic and high-enthalpy plasma wind tunnel (PHEDRA facility at ICARE laboratory, Orléans, France) to characterize high-density plasmas under re-entry-relevant conditions. The probes operated reliably despite exposure to high thermal fluxes (200 - 300 kW/m²), gas temperatures of several thousand kelvins, and potential erosion and corrosion. Thanks to a boron nitride protective coating, the probes sustained a cumulative plasma exposure of ~30 minutes, while maintaining full functionality. Experiments have demonstrated the usability of the curling probe diagnostic for re-entry ground campaigns, and suggested its potential for in-flight applications. Despite using microwave components not fully optimized for K-band operation, the diagnostic provided consistent measurements. Comparison with Langmuir probes has shown fair to good agreement across all tested conditions, supporting the accuracy and representativeness of CP measurements. Complementary DSMC simulations further confirmed that the probe response aligns with electron density distributions expected across the shock layer. Results indicate that the CP effectively measures the integral electron density over several millimeters across the shock layer, with values on the order of several  $10^{13}$  cm<sup>-3</sup>.

Overall, this study provides strong evidence that the curling probe can be reliably employed for high-density plasma characterization in re-entry conditions. Future work will focus on combining experimental measurements presented in this paper to refine DSMC simulations and derive more accurate neutral density distributions in the flow impinging on the model. This approach is particularly relevant because the measured electron densities imply ionization degrees of several tens of percent, raising questions about the reliability of pressure-based neutral density estimates. In parallel, improvements in probe hardware (particularly the use of fully K-band-compatible components),

enhanced CP design for improved accuracy, and alternative protective coatings will be pursued to further enhance diagnostic performance. Finally, it will be interesting to extend CP measurements to the free stream region.

# **Acknowledgements**

This research was supported by the Agence Nationale de la Recherche (ANR) and the Agence de l'Innovation de Défense (AID) under ASTRID project AMHYRA, grant number ANR-24-ASTR-0002. The authors would also like to thank Olivier de Bouët du Portal and Théo Delattre for their help during the experimental campaign.

#### References

- [1] L. C. Schroeder and N. D. Akey, "Material injection alleviation during the ram c-iii flight," *J. Spacecr. Rockets*, vol. 10, no. 3, pp. 170–174, 1973, doi: 10.2514/3.61866.
- [2] W. L. Grantham, "Flight results of a 25000-foot-per-second reentry experiment using microwave reflectometers to measure plasma electron density and standoff distance," 1970. [Online]. Available: https://ntrs.nasa.gov/citations/19710004000
- [3] C. Luo *et al.*, "Ground experimental study of the electron density of plasma sheath reduced by pulsed discharge," *Plasma Sources Sci. Technol.*, vol. 33, p. 095005, 2024, doi: 10.1088/1361-6595/ad75b3.
- [4] W. L. J. Jones and A. E. Cross, "Electrostatic-Probe Measurements of Plasma Parameters For Two Reentry Flight Experoments At 25000 Feet Per Second," 1972. [Online]. Available: https://ntrs.nasa.gov/citations/19720011555
- [5] A. Pandey, W. Sakakibara, H. Matsuoka, K. Nakamura, and H. Sugai, "Time-resolved curling-probe measurements of electron density in high frequency pulsed DC discharges," *Jpn. J. Appl. Phys.*, vol. 55, no. 1, 2016, doi: 10.7567/JJAP.55.016101.
- [6] F. Boni, J. Jarrige, V. Désangles, and T. Minea, "The curling probe: A numerical and experimental study. Application to the electron density measurements in an ECR plasma thruster," *Rev. Sci. Instrum.*, vol. 92, p. 033507, 2021.
- [7] F. Boni, J. Jarrige, and V. Désangles, "Real-time electron density measurement technique using a microwave resonant probe for low-pressure plasmas," *J. Phys. D. Appl. Phys.*, vol. 58, p. 09LT01, 2025.
- [8] F. Boni, V. Désangles, and J. Jarrige, "A sheath correction method for electron density measurements with the microwave resonant curling probe," *Plasma Sources Sci. Technol.*, vol. 32, no. 9, p. 095018, 2023, doi: 10.1088/1361-6595/acfb36.
- [9] M. Hotta, D. Ogawa, K. Nakamura, and H. Sugai, "Real-time curling probe monitoring of dielectric layer deposited on plasma chamber wall," *Jpn. J. Appl. Phys.*, vol. 57, p. 046201, 2018.
- [10] D. Ogawa, K. Nakamura, and H. Sugai, "A novel technique for in-situ simultaneous measurement of thickness of deposited film and electron density with two curling probes," *Plasma Sources Sci. Technol.*, vol. 29, no. 7, p. 075009, 2020.
- [11] F. Boni, J. Jarrige, and V. Désangles, "Plasma expansion and electron properties in a magnetic nozzle electrode-less thruster," in *37th International Electric Propulsion Conference*, Boston, Massachusetts, 2022, p. IEPC-2022-527.
- [12] N. Rembaut, "Rentrée atmosphérique de débris spatiaux: simulations expérimentales en souffleries hypersonique raréfiée et supersonique haute enthalpie," Université d'Orléans, 2021. doi: NNT: 2021ORLE3172.
- [13] V. Lago and A. A. Ndiaye, "Experimental investigation of supersonic low pressure air plasma flows obtained with different arc-jet operating conditions," in *AIP Conference Proceedings*, 2012, pp. 1423–1430. doi: 10.1063/1.4769706.
- [14] V. Lago, H. Noubel, C. Mélodie, J. Jonathan, and P. Juliette, "Modification of the bow shock shape and thermal effects with MHD actuator in supersonic low pressure plasma flows," in *HiSST: 2nd International Conference on High-Speed Vehicle Science Technology*, 2022, pp. 2022–414.
- [15] M. A. Lieberman and A. J. Lichtenberg, *Principles of plasma discharges and material processing*, 2nd Ed. Wiley, 2005.
- [16] S. J. Plimpton et al., "Direct simulation Monte Carlo on petaflop supercomputers and beyond," Phys. Fluids, vol. 31, p. 086101, 2019, doi: 10.1063/1.5108534.
- [17] "SPARTA web site." [Online]. Available: http://sparta.github.io
- [18] M. Pfeiffer, "An optimized collision-averaged variable soft sphere parameter set for air, carbon, and corresponding ionized species," Phys. Fluids, vol. 34, no. 11, p. 117110, 2022, doi: 10.1063/5.0118040.
- [19] K. Swaminathan-Gopalan and K. A. Stephani, "Recommended direct simulation Monte Carlo collision model parameters for modeling ionized air transport processes," *Phys. Fluids*, vol. 28, p. 027101, 2016, doi: 10.1063/1.4939719.
- [20] R. J. Gollan and P. A. Jacobs, "About the formulation, verification and validation of the hypersonic flow solver Eilmer," Int. J. Numer. Methods Fluids, vol. 73, pp. 19–57, 2013, doi: 10.1002/fld.3790.
- [21] P. A. Jacobs et al., The Eilmer3 Code: User Guide and Example Book 2015 Edition. 2015.